Novel Multi-Band Plasmon Filters based on Double-Band Surface Plasmon Polarizations

Abdollah Abertavi*, Masoud Jabbari, Ghahraman Solookinejad
Department of Electrical Engineering, Marvdasht Branch, Islamic Azad University, Marvdasht, Iran.
abartavi945555@gmail.com

Abstract

Surface plasmon polariton has been structured based on the surface electromagnetic excitation which belongs at the metal-air or metal-dielectric interface. Due to the augmented field and intense confinement near the metal surface, they present various applications from high sensitivity sensors to reduced photon components. In this pare, a Band-Pass Filter (BPF) based on designer-surface plasmon polarizations has been structured using central frequency and adjustable bandwidth. It has been adjusted via varactor diodes which are placed in different positions in the T-shaped resonator. Considering the constraints and strengthen high field surface plasmon polariton polarizations, hearing and coupling is less than the usual microstrip. Three inductors are considered at different locations of the T-shaped resonator which can be controlled by DC bias voltage. Transition from the quasi-transverse electromagnetic mode of the microstrip to the misleading mode of surface plasmon polariton has been performed to excite SSPP based on the T-shaped resonator with g-distance coupling.

Keywords: bandpass filter, adjustable central frequency, quasi-transverse electromagnetic, spoof surface plasmon polaritons,

1. Introduction

Surface plasmon polariton (SPP) has emitted an electromagnetic wave which happens at dielectric and conductor interface caused by the light coupling to collective electron oscillation [1]. As for its special feature, SPP let to break the diffraction constraint and light manipulation within sub-wavelength scales, and then strengthen the field concentration. Hence, SPP has been widely used in a wide variety of optical communication, photonic, and sensing fields [2-5].

SPP specific features such as slow-wave behavior and field limitations other than optical frequency regime make significant progress of components and devices. Due to natural occurrence of SPP in optical frequencies, different concepts are defined for SPP phenomenon in microwaves and terahertz frequency ranges. SSPP has mediated the surface electromagnetic waves disseminating through ridged metallic surfaces at frequency of microwave [6, 7].

Bandpass Filter (BPF) is the initial/final component of RF/microwave systems. Recent advances in demand for modern wireless communication and radar applications are high-performance, dynamic control RF

subsystems. Therefore, adjustable microwave filters are interesting for researchers and electronic engineers. The conventional microwave filters typically utilize traditional micro-strip technology which affects radiation loss, hearing loss, and interconnection problems. Alignment between transmission lines is involved in the results and signal accuracy which can reduce the quality of RF systems [8]. The spoof surface plasmon polaritons based on RF systems are alternative solution to overcome this problem [9, 10]. SPP is surface electromagnetic wave closely related to the consistent oscillations of the free-electron density at the interface in the middle of dielectric and metal material, whereas it is found at near-infrared and optical frequencies. They exponentially putrefy in the direction perpendicular to the surface of the interference in which to be revealed the constraint and increase of the field below the wavelength [11, 12].

Because metal behaves like plasma with a negative transmittance at the light frequency, the SPP wave is supported by a metal-dielectric interference surface. However, metals exhibit properties such as a full conductor at microwave and terahertz frequencies. Therefore, exotic properties are not usually found in this frequency range. Recently, it has been revealed that semi-metals such as graphene and semiconductors have naturally supported SPPs at terahertz which can be used in optoelectronic devices such as solar cells, graphene as sensors, and also other nanophotonic and plasmonic devices [13-15].

However, to understand the SPP-like properties in the closeness of the metal-dielectric interference surface at microwave and terahertz frequencies, plasmonic metamaterials [16] which are proposed as ultra-long wavy metal surfaces with 2-dimensional cavities or 1-dimensional grooves is called SPP maker. The scattering curve and cutoff frequency for such a structure can be modified by physical parameters. Thus, these structures can conduct and manipulate electromagnetic waves at the sub-wave scale, which can be used to design transmission lines [17, 18] and filters [19-21], withal to excite antennas [22], amplifiers [23], terahertz switches [24] and adjustable filters [25-29].

In [25, 28], an adjustable band-stop behavior has been analyzed via changing the physical dimensions. In [26], a new spoof surface plasmon transmission line (SSP-TL) is proposed based on capacitor loading technique which make it more flexible and adaptive dispersion control which requires reduced line-width as compared to its conventional type to achieve an very slow wave and quietly applicable for compact systems. Even so, the presented structure in [25-27, 30] requires manual time adjustment with different parameter values to belong adjustable feature. In [29], an adjustable band-pass filter is proposed based on transmission lines to control the low-high cut-off frequencies of the filter which is too large and complex for the operational prototype.

In this regard, this paper aims to design a new a two-layer and one-sided wavy-based BPF structure to transfer multiple bands. The cut-off frequency of all bands depends on different modes of approximate frequency of SSPPs which can be easily adjusted by the depth of the grooves. The proposed structure can be adjusted using varactor diodes which are placed in different positions in the T-shaped resonator. Considering

the constraints and strengthen high field surface plasmon polariton polarizations, hearing and coupling is less than the usual microstrip. Three inductors are considered at different locations of the T-shaped resonator which can be controlled by DC bias voltage. Transition from the quasi-transverse electromagnetic mode of the microstrip to the misleading mode of surface plasmon polariton has been performed to excite SSPP based on the T-shaped resonator with g-distance coupling.

2. Surface Polariton Plasmon and Its Stimulation Strategy

Plasmon in the classical image is the mass oscillation of free electrons which is described with respect to the constant positive ions in a metal. The surface plasmon polaritons are surface electromagnetic waves that propagate along the interference surface between a metal and a dielectric material that the electromagnetic waves include surface charges. The first question is how to excite the surface loads? A polarized wave p reaches a flat interference plane at the collision angle θ_1. The shock wave has a photon momentum $\hbar k_d$ in the dielectric with a refractive index n_d. When the wave reaches the interference surface, it is propagated by reflecting waves at angles equal to the incident angle, and the momentum of the photons remains constant. In addition, the wave propagates in the metal in a new direction with a refractive angle θ_2. The photon momentum is $\hbar k_m$, whereas $k_m=2\pi n_m/\lambda$ and n_m is the refractive index of the metal, and the momentum components are constant along the x direction. Let $k_{dx}=k_{mx}$ that $k_{dx}=k_d*\sin\theta_1$ and $k_{mx}=k_m*\sin\theta_2$. The Snell's law can be presented as follows:

$$\boldsymbol{n_d \sin \theta_1 = n_m \sin \theta_2} \quad (1)$$

In general, the dielectric refractive index n_d is larger than the metal type n_m in visible spectrum [31]. Since $n_d>n_m$, the maximum value of θ_2 is 90°, and θ_1 is restricted. Beyond the angle limit, the wave cannot propagate through the metal, in which case the limited impact angle is called the critical angle θ_c that: $\sin\theta_c=n_m/n_d$.

The momentum of a wave along the surface with an angle of impact higher than θ_c is greater than what can be supported by metal. For p-polarized impact waves on the surface, the oscillating electric field creates surface charges at the interfering surface of the metal and dielectric, and the surface charges will be under a collective oscillation. Although the wave is completely reflected on the interference surface, due to the oscillating loads, the radiation fields penetrate into the metal. The evanescent fields are perpendicular to the interference surface.

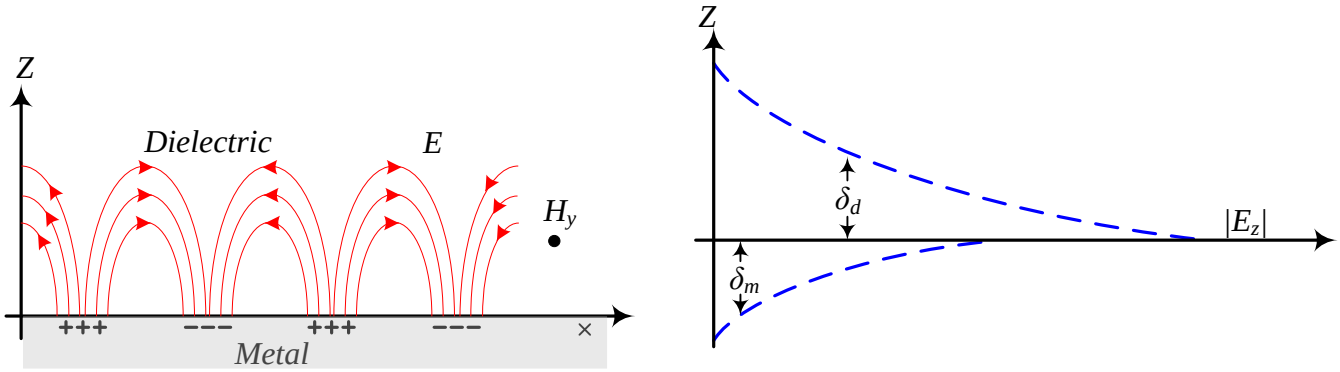

Figure 1. Schematic of the surface plasmon polaritons propagation between metal and air.

At the critical angle, the decremental length goes to infinity, but as the angle further increases, it rapidly decreases to the light wavelength. In these cases, the evanescent fields are more suitable for the incidence wave than the critical angle for the radiation coupling with the SPPs.

Since there is no vertical boundary on E_x, this component is fixed along the boundary. However, in the case of E_z there is no component perpendicular to E, D_z is a continuous component of D (there is no free charge), and E_z has to change if ε changes because: $D_z=\varepsilon_d\varepsilon_0$ and $E_{zd}=\varepsilon_m\varepsilon_0 E_{zm}$. This discontinuity in E_z leads to polarized loads at the interference surface. From these simple assumptions, it is clear that polarized impact radiation does not normally cause load on an interfering surface. P-polarized wave automatically generates time-dependent polarized loads on the interfering surface. Being vertical E fields are needed to create surface charges; it is essential to consider P-polarized electromagnetic waves. In addition, the surface wave in any form must satisfy the electromagnetic wave equation in the two materials. If the plane x-y is an interference plane, for the wave propagated in the x direction as z> 0:

$$E_d = (E_{xd}.\,0.\,E_{zd})\exp(-k_{zd}z)\exp[i(k_x x-\omega t)]$$
$$H_d = (0.\,H_{yd}.\,0)\exp(-k_{zd}z)\exp[i(k_x x-\omega t)] \quad (2)$$

When z <0, and also:

$$E_m = (E_{xm}.\,0.\,E_{zm})\exp(-k_{zm}z)\exp[i(k_x x-\omega t)]$$
$$H_m = (0.\,H_{ym}.\,0)\exp(-k_{zm}z)\exp[i(k_x x-\omega t)] \quad (3)$$

Using Eq. 2 and Eq. 3 in Maxwell's equation, ∇·E=0, the components of the electric field can be presented as follows:

$$E_{zd} = i\frac{k_x}{k_{zd}}E_{xd}$$
$$E_{zm} = -i\frac{k_x}{k_{zm}}E_{xm} \quad (4)$$

With considering Eq. 2 and Maxwell equation in the form $\nabla\times E=-c^{-1}\partial H/\partial t$:

$$-k_{zd}E_{xd} - ik_xE_{zd} = ikH_{yd} \quad (5)$$

$$k_{zm}E_{xm} - ik_xE_{zm} = ikH_{ym}$$

That finally Eq. 6 can be attained:

$$\varepsilon_d kE_{xd} = ik_{zd}H_{yd} \quad (6)$$

$$\varepsilon_m kE_{xm} = -ik_{zm}H_{ym}$$

Where:

$$k_{zd}^2 = k_x^2 - \varepsilon_d k^2 \quad (7)$$

$$k_{zm}^2 = k_x^2 - \varepsilon_m k^2$$

In addition, I must note that the tangent components E and H are continuous according to the boundary conditions of the electromagnetic fields at z=0, i.e. $E_{xd}=E_{xm}$ and $H_{yd}=H_{ym}$, The relationship between the dielectric constants and the normal components of the wave vector will be in two space: $k_{zd}/k_{zm}=-\varepsilon_d/\varepsilon_m$. Then:

$$k_x = k\sqrt{\frac{\varepsilon_d\varepsilon_m}{\varepsilon_d + \varepsilon_m}} \quad (8)$$

Considering k_{xpp} instead of k_{xpp}, SPP scattering equation can be presented as follows:

$$k_{SPP} = k\sqrt{\frac{\varepsilon_d\varepsilon_m}{\varepsilon_d + \varepsilon_m}} \quad (9)$$

The SPP scattering curve shows nonlinear properties, which are portrayed in the Figure 2.

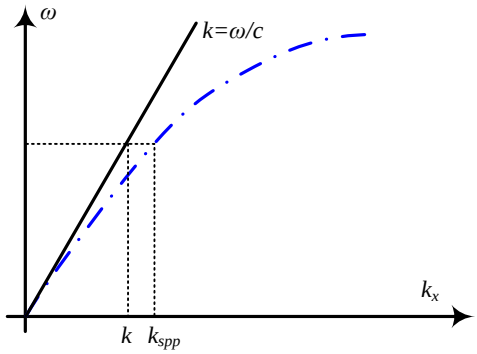

Figure 2. The scattering curves of a SPP wave

$\hbar k_{spp}$ momentum of SPP wave is greater than the momentum of light in open space photons ($\hbar k$) for the same frequency (ω) which causes the momentum mismatch between light and SPP. This mismatch must be overcome by coupling the SPP and light modes at the interference surface when $\varepsilon_d+\varepsilon_m=0$.

Surface loads generate mass oscillations to excite SPPs. The dielectric constant of the metal ε_m has the shape of a free electron:

$$\varepsilon_m = 1 - \frac{\omega_p^2}{\omega^2} \tag{10}$$

Where, ω_p is the bulk plasma frequency. For many metals, the frequency is in the ultraviolet wavelength range, whereas metal is not above that frequency. According to Eq. 10, SPP frequency can be attained by:

$$\omega_{spp} = \frac{\omega_p}{\sqrt{1+\varepsilon_d}} \tag{11}$$

It can be seen that the SPP frequency is lower than the bulk plasma frequency.

Excitation of the SPPs described above occurred at a single-surface of interference between the dielectric and the metal. In contrast, a thick metal film bounded by a dielectric can excite two independent SPP waves at two surfaces including dielectric and metal. In this case, the evanescent fields of the two non-coupled SPP waves inside the metal cannot overlap [3]. In case of thin enough metal film, the evanescent fields of the two SPP waves inside the metal can overlap, and two SPP waves coupled between the two intervening surfaces appear. As a result, SPP waves are converted into two super-mods (coupled modes) including a symmetric mode (low frequency) and an asymmetric mode (high frequency) with a transverse electric field distribution. Figure 3 shows the metal bound between the dielectric and the dielectric between the sheet metal and the excitation state of SPP in both cases.

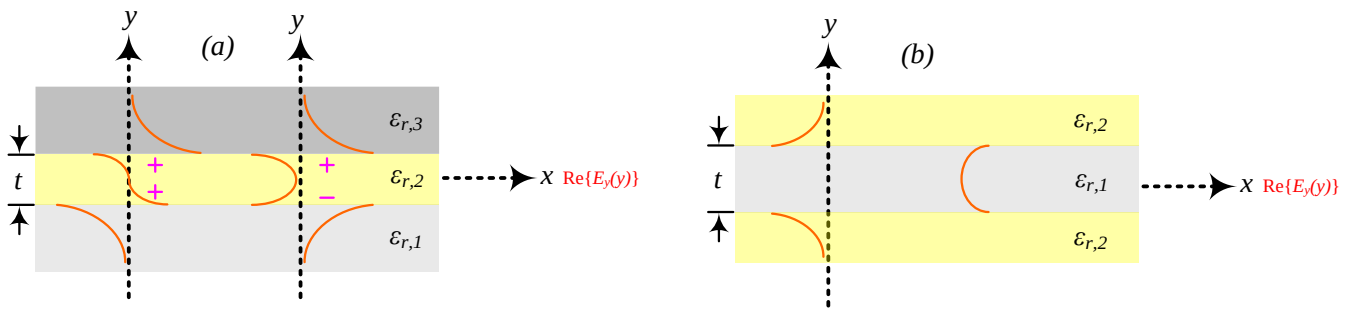

Figure 3. (a) The metal sheet ($\varepsilon_{r,2}$) and thickness t bounded by semi-infinite dielectrics ($\varepsilon_{r,1}$, $\varepsilon_{r,3}$) and support two modes of SPP (a_b, s_b). (b) A dielectric sheet ($\varepsilon_{r,1}$) with thickness t bounded by semiconductor metals ($\varepsilon_{r,2}$) and supports a symmetric bound mode.

Thus, the electric field drop is very small in the symmetric SPP mode, because the electric fields penetrate deep into the dielectric, and the attenuation of the electric fields is much less than that of the SPP at the single interference surface. Thus, the symmetric SPP mode is also called the long-range SPP (LRSPP) that its LRSPP propagation length is also very long, 138 times longer than the individual SPP [32]. However, the electric field drop is very large in the asymmetric SPP mode, because the electric fields are primarily concentrated within the metal and the SPP modes show increasing limitations. Thus, the asymmetric SPP mode is basically called short-range SPP (SRSPP), and the propagation length is very short due to the very strong damping (strong ohmic drops) in the metal [33].

3. Theory and Principle of Multi-Band Plasmon Filter

In this work, a BPF based on designer-surface plasmon polarizations has been structured using central frequency and adjustable bandwidth which can be adjusted using varactor diodes and placed in different positions in the T-shaped resonator. The theory and principles of the proposed filter has been here explained.

3.1. Design theory and principles

Figure 4 shows the T-shaped resonator of the SPP along with the equivalent circuits to odd and even modes. This T-shaped resonator can be provided as two $\lambda_g/4$ resonators coupled via the K inverter provided by the SSPP transmission line section. The electrical length (degree) and the conductance (1/Ω) are in one part of the line ($\varphi_1/2$, Y_1) and another line (φ_k, Y_1). Each wavy transmission line with metal strips on it has an electrical length and conductance $\Delta\varphi'$ and $\Delta Y'$. By adjusting the taps' length which can be longer or shorter than $\lambda_g/4$, a zero transmission can be generated at a frequency lower or higher than the desired pass band. Since the groove length is less than $\lambda_g/4$, thus, a zero transmission is produced in the higher stop band.

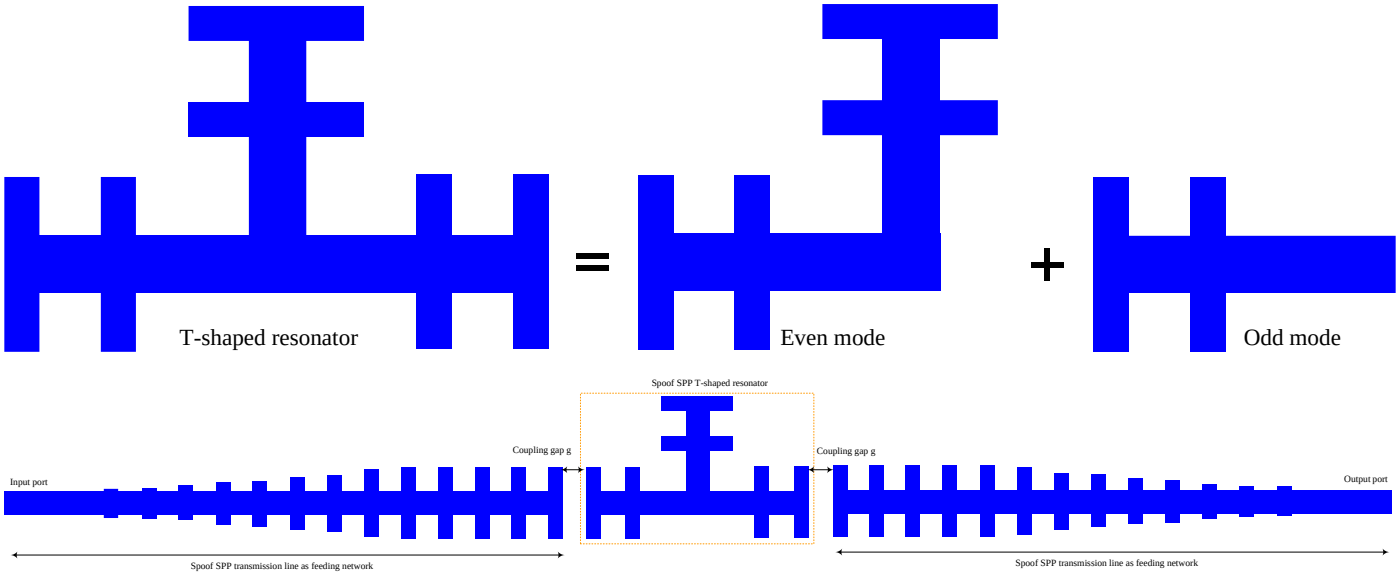

Figure 4. T-shaped resonator of the SPP along with the equivalent circuits to odd and even modes.

In the designed resonator, the resonance condition is defined as follows:

$$Img[Y_{ine}] = 0 \tag{12}$$

Where, Y_{ine} is the conductance of even mode which is defined by:

$$Y_{ine} = Y_1\left[\frac{Y_M + jY_1\tan(\emptyset_1/2)}{Y_1 + jY_M\tan(\emptyset_1/2)}\right] + n^*(jY'\tan\Delta\emptyset') \tag{13}$$

$$Y_M = j\frac{Y_1}{2}\tan\emptyset_k + m^*(j\Delta Y'\tan\Delta\emptyset')$$

$$Img[Y_{ino}] = 0$$

Where, n = 4 and m = 2. Y_{ino} is the conductance of an individual mode which is defined by:

$$Y_{ino} = -j\,Y_1 \cot\left(\frac{\Phi_1}{2}\right) + n^*(\Delta Y' \tan \Delta \emptyset') \quad (14)$$

As for Eq. 12 and Eq. 13, it is clear that φ_1 affects both even and odd modes, whereas While φ_k only affects the even mode. Therefore, by adjusting the physical length, the equivalent electrical path for different frequency and even state frequencies can be changed.

3.2. Power supply network design

The SSPP T-shaped resonator is directly coupled to the power supply transition line of the SPP at the input and output of Figure 4. This transmission line must contain cellular arrays. The behavior of SSPPs has been analyzed by scatter plots. The emission characteristics of SSPP guided modes can be controlled by its structural parameters including distance between two grooves d, groove height h, metal thickness t and p lattice constant. Dispersion properties of the SSPP unit cell have been obtained by numerical simulation using CSTMWS.

3.3. Design of SSPP T-shaped resonator with odd-even mode analysis

Figure 5 shows a schematic of the proposed adjustable T-resonator with an odd-even mode equivalent circuit. Two varactor diodes (C) and one varactor diode (C1) are symmetrically placed in the X and Y directions and on the XY plane in the resonator.

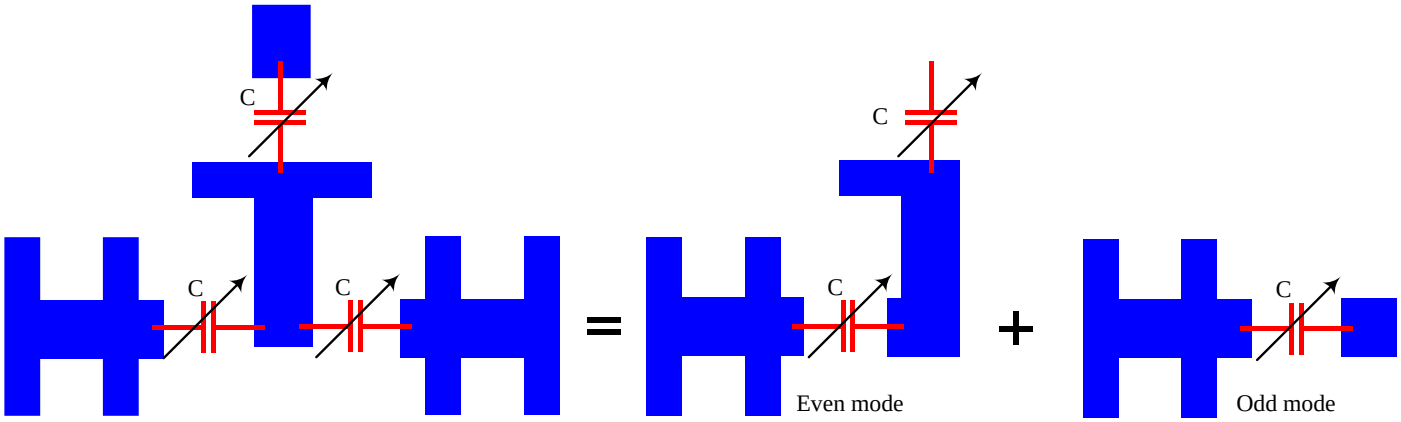

Figure 5. Schematic of the proposed adjustable T-resonator with an odd-even mode equivalent circuit

Resonance schemes for the proposed resonator can be obtained by:

$$Img[Y_{ine}] = 0 \quad (15)$$

$$Img[Y_{ino}] = 0$$

Where, Y_{ine} and Y_{ino} are respectively the conductance of even and odd modes, respectively that are defined as follows:

$$Y_{in} = Y_1 \left[\frac{Y'_M + jY_1 \tan(\emptyset_A)}{Y_1 + jY'_M \tan(\emptyset_A)}\right] + n^*(j\Delta Y' \tan \Delta\emptyset') \quad (16)$$

Where, $Y_{ine}=Y_{in}$ in case of:

$$Y'_M = \frac{Y_M * jwC}{Y_M + jwC}$$

$$Y_M = \frac{Y_1}{2}\left[\frac{jw\,C_1/2 + j\frac{Y_1}{2}\tan(\emptyset_k)}{\frac{Y_1}{2} + j(jw\,C_1/2\tan(\emptyset_k)}\right] + (j\Delta Y' \tan \Delta\emptyset') \quad (17)$$

Where, $Y_{ino}=Y_{in}$ while $Y'_M=j\omega C$.

For odd and even mode admissions, the conductance matrix can be expressed as follows:

$$Y = \begin{bmatrix} Y_{11} & Y_{12} \\ Y_{21} & Y_{22} \end{bmatrix} = \begin{bmatrix} \frac{(Y_{ine} - Y_{ino})}{2} & \frac{(Y_{ine} + Y_{ino})}{2} \\ \frac{(Y_{ine} + Y_{ino})}{2} & \frac{(Y_{ine} - Y_{ino})}{2} \end{bmatrix} \quad (18)$$

In addition, the transmission zeros are expressed in the conductance parameter terms as follows:

$$Y_{12} = Y_{21} = (Y_{ine} + Y_{ino})/2 = 0 \quad (19)$$

According to Eq. 15, the varactor (C) affects both odd and even modes, whereas the varactor (C_1) affects only the even mode. Because varactor C affects both odd and even modes simultaneously, whereas the central frequency of the degenerative mode can generally be varied by changing the bias voltage around varactor C.

The way is that, V_{C1} is essentially considered constant and the bias voltage (V_C) around the varactor C changes, in which case the central frequency will be shifted. Then, V_C is considered constant, and the bias voltage of diodes C_1 changes. Since C_1 only affects the even mode wave, the degenerative mode splits and the bandwidth is adjusted.

Also, modulation analysis is performed to design the BPF. The signal distortion based on two-tone method is proposed for it [34]. The simulated modulation product is obtained by using ADS harmonic equilibrium simulation around the lowest frequency f_0 of the adjustable region. The two cases are distinguished by Δf which are located at the frequencies $f_1=f_0-\Delta f/2$ and $f_2=f_0+\Delta f/2$.

4. Simulation Results of Discussion

Power supply network design results

The T-shaped resonator is directly connected to the SSPP transmission line at the input and output as shown in Figure 4. This transmission line contains alternating arrays of unit cell shown in Figure 6. The SSPP behavior is portrayed by the scattering diagram, where the blue line indicates the emission wave vector (k_0)

for the freely propagated wave and the green curve indicates the emission wave vector (k_y) for the SSPP unit cell.

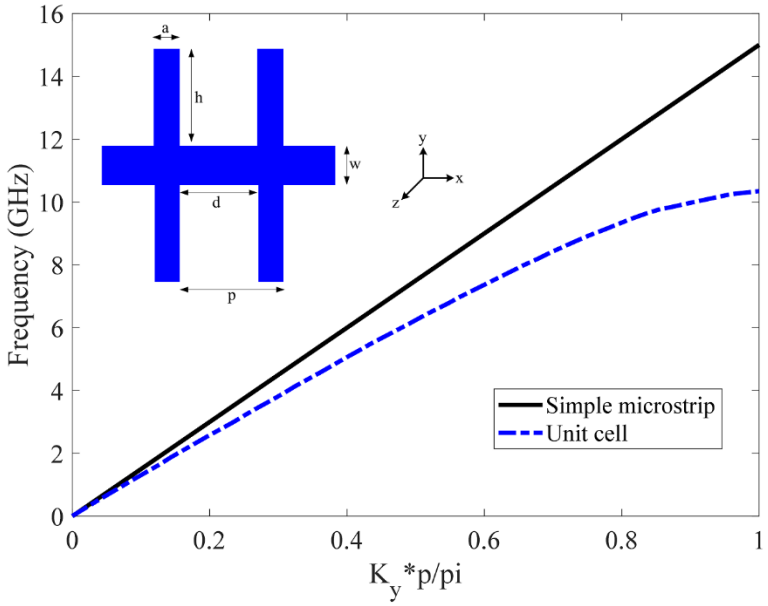

Figure 6. Dispersion curves of SSPP unit cell with bilateral grooves

The propagation properties of the guided modes can be controlled by its structural parameters including distance between two grooves *d*, groove height *h*, metal thickness *t* and lattice constant *p*. Since k_y deviates from k_0, there is a mismatch between their momentum and polarization. This mismatch leads to low productivity, so a conversion area must be designed to achieve a gradual conversion, as shown in Figure 7.

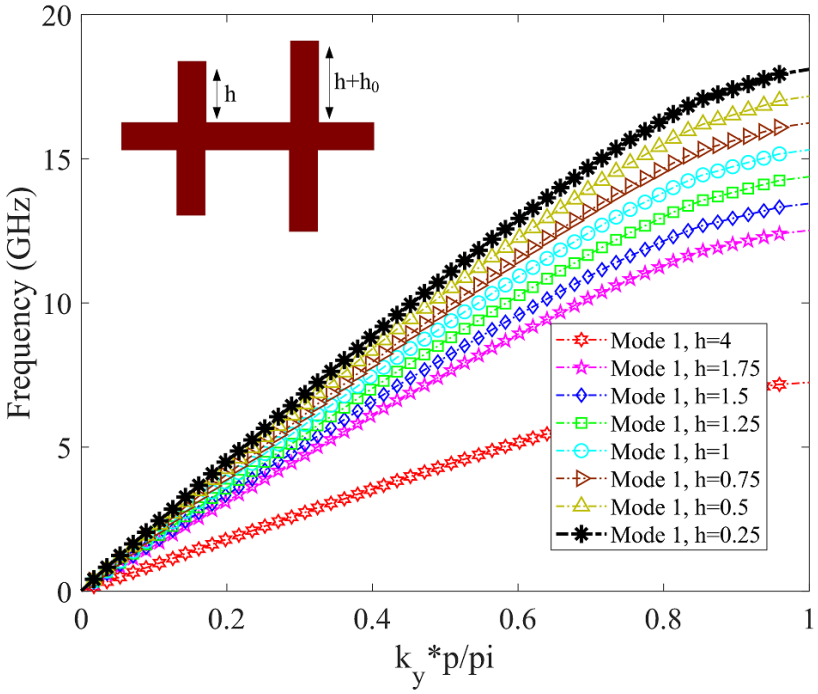

Figure 7. Dispersion curves associated with gradual conversion in a SSPP unit cell

As shown in Figure 7, the grooves height varies from h_1 to h_8 with equal steps which leads to relative adaptations between the wave vectors.

On the other hand, the designed filter has a dual-mode frequency response for each parametric analysis with respect to l_l and l_k in electromagnetic simulations. To attain the relevant results, first l_l is changed by means of l_k whereas keep the rest of the physical parameters constant. Both odd and even modes change, so the center frequency has moved downward.

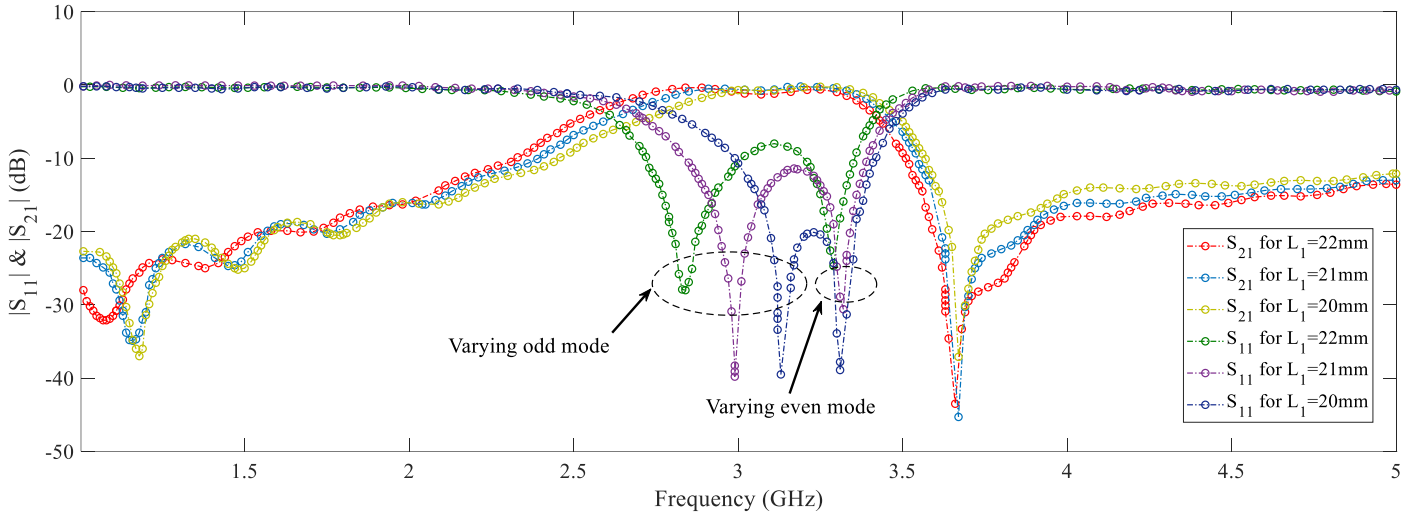

Figure 8. S Simulation of T-shaped resonator based on the BPF with respect to the l_l variation.

According to Figure 8, both odd and even modes have been changing. In the Figure 8, l_k is changed by l_l whereas other physical parameters are constant.

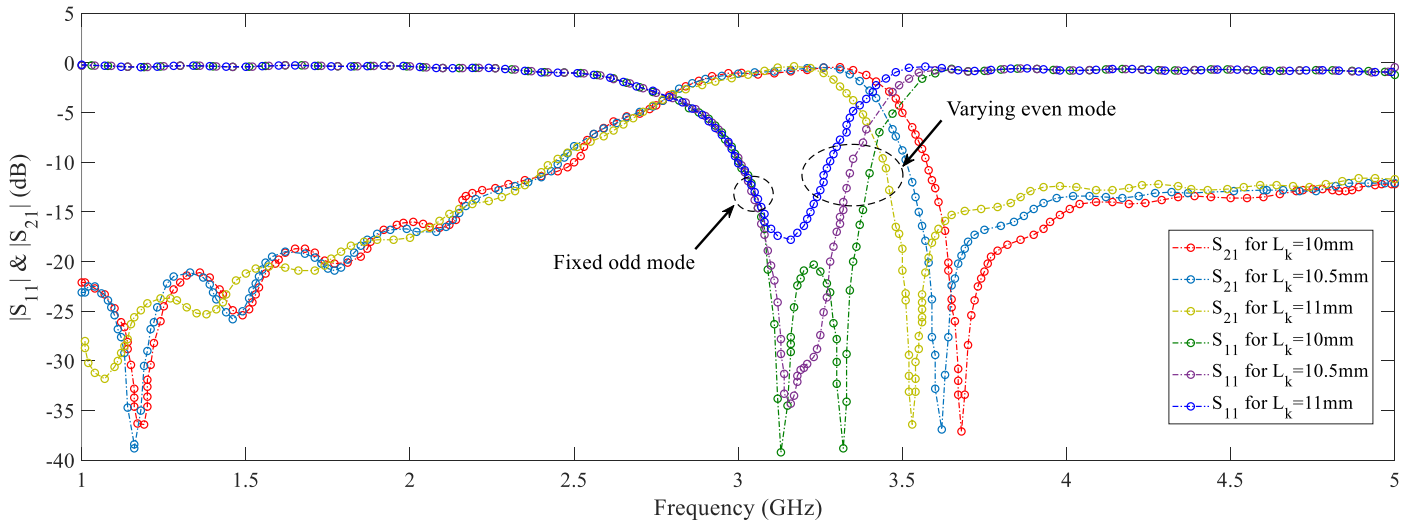

Figure 9. S Simulation of T-shaped resonator based on the BPF with respect to the l_k variation.

As shown in Figure 9, the odd mode is fixed at a specific frequency, but the even mode moves to lower frequencies. Hitherto, the conditions of the modes have bed examined, and then the reflection and passage coefficients have been examined for the designed BPF with different distances g.

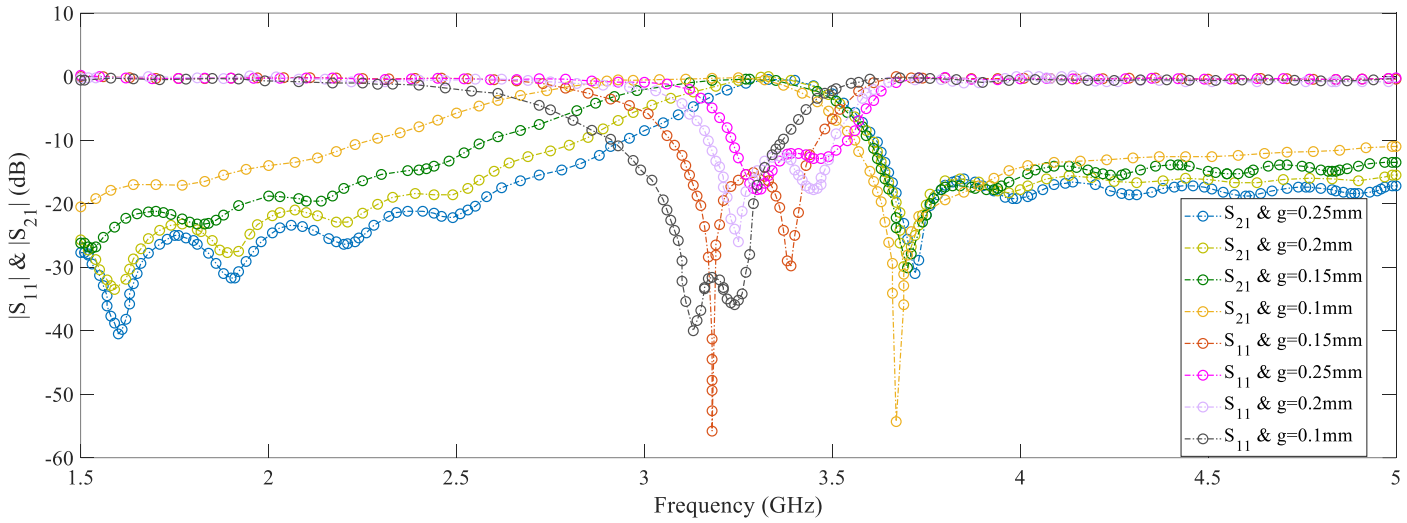

Figure 10. S Simulation of T-shaped resonator based on the BPF with respect to different distances g.

As shown in Figure 10, the property of each parameter S is obtained with four different distances. It can be seen that as the coupled distance increases, the input-output connection decreases due to the small capacity of the distance as a result of poor matching. To more verify the performance of the proposed scheme, it has been compared with the previous works which are presented in Table 1.

Table 1: Comparison of different situations for plasmonic filters

Reference	Cost-price	Tuning method	Tuning parameter	Method	Description
[15]	High	Static tune	Bandwidth	Bandwidth of the band stop is tuned based on graphene tunable sensor.	A graphene-based suspended nano-strip line is implemented for the integrated circuits at terahertz frequencies.
[35]	High	Static tune	Central frequency	The central frequency is tuned by changing the dimensions of the unit cell.	Thin band-stop and multiple band-stop filters are obtained using CPW based on metal plasmonic waveguides which support SSPP.
[16]	High	Static tune	Cut-off frequency	Change of capacity value to attain scattering, cut-off frequency and operating band frequency characteristics	Capacitor of SSPP is to attain the scattering reset capability and filtering properties.
[17]	High	Dynamic tune	Central frequency	Variable capacitive components have been taken into the SSPP unit cell.	Bandwidth characteristics of the SSPP unit cell have been tuned.
This paper	Low	Dynamic tune	Central frequency and bandwidth	Reactors in T-shaped resonator structure to control single and even frequency modes	Central frequency and BPF tunable bandwidth using T-shaped resonator based on SSPP

Alternating grooves with metal substrate support SSPP waves. Using impedance matching theory, a strip SSPP structure has been designed by converting the performance of traditional micro-strip lines and an SSPP structure using corrugated grooves. The simple meta-material between the SSPP and its wave field is returned due to the high electric field intensity under the toothed parts of SSPP strip section. This type of

SSPP structure is feasibly to design and construct. As for the performed analysis in this paper, high efficiency of SSPP waves is revealed which can be a valuable guide to develop the SSPP circuits.

5. Conclusion

In this study, spoof plasmonics based band-pass filter using T-shaped resonator is proposed and structured by means of simultaneous resetting the central frequency and bandwidth. The proposed filter has proved to be superior than other plasmonic filters which have been compared with each other. It can accurately work by tuning the dynamics along with the central frequency and bandwidth of the meta-material filter. The simulation results revels that the central frequency moves downwards and also the settlement between the s parameters in different modes is achieved. Therefore, the suggested frequency spectrum tunable SSPP filter can presents a significant performance and flexibility which is practicable to be applied in advanced intelligent systems.

6. References

[1] G. Challa Ram, P. Sambaiah, S. Yuvaraj, M.V. Kartikeyan, “Graphene based filter design using triangular patch resonator for THz applications”, Nano Communication Networks, Vol. 38, 2023, pp. 100477.

[2] S. Jain, K. Choudhary, S. Kumar, “Photonic crystal fiber-based SPR sensor for broad range of refractive index sensing applications”, Optical Fiber Technology, Vol. 73, 2022, pp. 103030.

[3] L. Hajshahvaladi, H. Kaatuzian, M. Danaie, “A very high-resolution refractive index sensor based on hybrid topology of photonic crystal cavity and plasmonic nested split-ring resonator”, Photonics and Nanostructures - Fundamentals and Applications, Vol. 51, 2022, pp. 101042.

[4] E.P. Rodrigues, A.A. Melo, A.M.N. Lima, “Predicting the Performance of Surface Plasmon Resonance Sensors Based on Anisotropic Substrates”, Plasmonics Vol. 16, No. 2, 2021, pp. 403–412.

[5] F.H. Suhailin, A. A. Alwahib, Y.M. Kamil, “Fiber-based Surface Plasmon Resonance Sensor for Lead Ion Detection in Aqueous Solution” Plasmonics Vol. 15, No. 3, 2020, pp. 1369–1376.

[6] M. A. Unutmaz, M. Unlu, “Fixed physical length spoof surface plasmon polariton delay lines for a 2-bit phase shifter”, Journal of the Optical Society of America B, Vol. 37, No. 4, 2020, pp. 1116-1121.

[7] L. Z. Yin, T. J. Huang, F. Y. Han, J. Y. Liu, D. Wang, P. K. Liu, “High-efficiency terahertz spin-decoupled meta-coupler for spoof surface plasmon excitation and beam steering”, Optics Express, Vol. 27, No. 13, 2019, pp. 18928-18939.

[8] D. A. Hill, R. T. Johnk, “Crosstalk between microstrip transmission lines”, IEEE Transactions on Electromagnetic Compatibility, Vol. 36, No. 4, 1994, pp. 314-321.

[9] B. Camli, A. D. Yalcinkaya, “Resonant Type RF Glucose Biosensors”, Encyclopedia of Sensors and Biosensors, Vol. 3, 2023, pp. 308-331.

[10] H. Tian, G. Huang, F. Xie, W. Fu, X. Yang, “THz biosensing applications for clinical laboratories: Bottlenecks and strategies”, TrAC Trends in Analytical Chemistry, Vol. 163, 2023, pp. 117057.

[11] J. Akbar, A. Khan, M. Abdul, L. Hou, “Manipulation of surface plasmon polariton fields excitation at quantum-size slit in a dielectric and graphene interface”, Optics & Laser Technology, Vol. 170, 2024, pp. 110234.

[12] P. Lingos, G. Perrakis, O. Tsilipakos, G. D. Tsibidis, E. Stratakis, “Impact of plasmonic modes on the formation of self-organized nano-patterns in thin films”, Optics & Laser Technology, Vol. 163, 2023, pp. 109415.

[13] V. M. Agarwal A, Viti L, Cupolillo A, Politano A, “Plasmonics with two-dimensional semiconductors: from basic research to technological applications.,” Nanoscale, Vol. 10, No. 19, 2018.

[14] J. Zhang, Z. Guan, K. Ma, D. Teng, “Perovskite nanowires-based graphene plasmonic waveguides with low loss and low gain threshold”, Diamond and Related Materials, Vol. 140, 2023, pp. 110540.

[15] R. S. Singh, P. K. Sarswat, “From fundamentals to applications: The development of magnetoplasmonics for next-generation technologies”, Materials Today Electronics, Vol. 4, 2023, pp. 100033.

[16] Y. Liang, H. Yu, H. Wang, H. C. Zhang, T. J. Cui, “Terahertz metadevices for silicon plasmonics”, Chip, Vol. 1, No. 4, 2022, pp. 100030.

[17] J. Wei, W. Li, L. Y. Niu, S. Gao, T. J. Cui, W. Tang, “Bendable transmission line and amplifier of spoof surface plasmon polaritons at microwave frequencies”, Opt. Express, Vol. 31, 2023, pp. 755-764.

[18] R. S. Anwar, H. Ning, L. Mao, “Recent advancements in surface plasmon polaritons-plasmonics in subwavelength structures in microwave and terahertz regimes”, Digital Communications and Networks, Vol. 4, No. 4, 2018, pp. 244-257.

[19] J. Luo, J. He, A. Apriyana, G. Feng, Q. Huang, Y. P. Zhang, “Tunable Surface-Plasmon-Polariton Filter Constructed By Corrugated Metallic Line and High Permittivity Material”, IEEE Access, Vol.. 6, 2018, pp. 10358-10364.

[20] A. Siemion, “Terahertz Diffractive Optics—Smart Control over Radiation”, Journal of Infrared, Millimeter, and Terahertz Waves, Vol. 40, 2019, pp. 477-499.

[21] S. Zhao, J. Zhao, W. X. Tang, “An ultra-compact rejection filter based on spoof surface plasmon polaritons”, Scientific Reports, Vol. 7, No. 1, 2017, pp. 10576.

[22] R. K. Jaiswal, N. Pandit, N. P. Pathak, “Design, Analysis, and Characterization of Designer Surface Plasmon Polariton-Based Dual-Band Antenna”. Plasmonics, Vol. 13, No. 1, 2018, pp. 1-10

[23] A. Farmani, A. Omidniaee, “Observation of Plasmonics Talbot effect in graphene nanostructures”, scientific reports, Vol. 14, 2024, pp. 1973.

[24] S. Gong, C. Bi, L. Wang, H. Zeng, F. Lan, Z. Yang, Y. Zhang, “Dynamic terahertz transmission based on coupling reconfiguration of spoof surface plasmon polaritons”, Opt. Express, Vol. 30, 2022, pp. 41264-41270.

[25] A. K. Varshney, N. P. Pathak, D. Sircar, “Low-profile metasurface-based dual-band graphene patch nanoantenna”, Nano Communication Networks, Vol. 35, 2023, pp. 100428,.

[26] X. Tang, S. Hu, A. Kandwal, T. Guo, Y. Chen, “Capacitor-loaded spoof surface plasmon for flexible dispersion control and high-selectivity filtering,” IEEE Microwave and Wireless Components Letters, Vol. 27, No. 9, pp. 806-808, 2017.

[27] “Ultra-compact spoof surface plasmon polariton waveguides and notch filters based on double-sided parallel-strip lines”, Journal of Physics D: Applied Physics, L. Ye, H. Feng, W. Li, Q. H. Liu, Journal of Physics D: Applied Physics, Vol. 53, No. 26 2020, pp. 265502.

[28] B. Xu, Z. Li, L. Liu, J. Xu, C. Chen, C. Gu, “Bandwidth tunable microstrip band-stop filters based on localized spoof surface plasmons”, Journal of the Optical Society of America B, Vol. 33, No. 7, 2016, pp. 1388-1391.

[29] H.C. Zhang, X. Gao, W. X. Tang, T. J. Cui, “Pass-band reconfigurable spoof surface plasmon polaritons”, Journal of Physics: Condensed Matter, Vol. 30, No. 13, 2018, pp. 134004.

[30] J. A. Brown, S. Barth, B. P. Smyth, A. K. Iyer, Compact Mechanically Tunable Microstrip Bandstop Filter With Constant Absolute Bandwidth Using an Embedded Metamaterial-Based EBG, IEEE Transactions on Microwave Theory and Techniques, Vol. 68, No. 10, 2020, pp. 4369–4380.

[31] P. E. D, “Handbook of Optical Constants of Solids”, New York: Academic, p. 275, 1985.

[32] Z. Chen, I. R. Hooper, J. R. Sambles, “Coupled surface plasmons on thin silver gratings”, Journal of Optics A: Pure and Applied Optics, Vol. 10, No. 1, 2007, pp. 015007.

[33] E. Sargent, “Colloidal quantum dot solar cells”, Nature Photon, Vol. 6, 2012, pp. 133–135.

[34] L Dussopt, “Intermodulation distortion and power handling in RFMEMS switches, varactors and tunable filters”, IEEE Transactions on Microwave Theory and Techniques, Vol. 51, No. 4, 2003, pp. 1247–1256.

[35] AK Varshney, D. Sircar, “Design of graphenebased THz antennas”, Proceedings of ICCASP, Advances in Intelligent Systems and Computing, 2019, pp. 29-35.